Dynamic imaging with x-ray holography

Felix Büttner

Dynamic Imaging with X-ray Holography

Felix Büttner

Additional information is available at the end of the chapter

Abstract

X-ray holography is a type of coherent diffractive imaging where the phase information is physically encoded in the diffraction pattern by means of interference with a reference beam. The image of the diffracting specimen is obtained by a single Fourier transform of the interference pattern. X-ray holography is particularly well-suited for high resolution dynamic imaging because, intrinsically, the reconstructed image does not drift and the images show high contrast. Therefore, the motion of features between two images can be determined with a precision of better than 3 nm, as demonstrated recently. In this chapter, the technical aspects of X-ray holography are discussed from an end user perspective, focusing on what is required to obtain a high quality image in a short time. Specifically, the chapter discusses the key challenges of the technique, such as sample design and fabrication, beam requirements, suitable end stations, and how to implement pump-probe dynamic imaging. Good imaging parameters were found using simulations and experiments, and it is demonstrated how a deviation from the optimum value affects the image quality.

Keywords: X-ray holography, high resolution imaging, dynamic imaging, magnetic imaging, soft X-ray imaging

1. Introduction

X-ray imaging is one of the work horses of modern science, at least since the availability of brilliant and coherent light at accelerator radiation sources of the third and fourth generation. X-ray imaging can yield excellent spatial resolution due to the short wavelength of the light and provides a great depth of information of the electronic state of the imaged specimen via spectroscopy. In addition, synchrotron X-ray photons typically come in short pulses, which facilitates time-resolved imaging. Manifold techniques exist for X-ray imaging, each with its merits and constraints. X-ray holography is one of these techniques for imaging of the real space electronic structure with particular strengths in applications requiring drift-free

imaging (a merit that is derived from Fourier space imaging because drift in Fourier space translates to phase shifts in real space) and in situ sample manipulations.

Using holography for soft X-ray imaging, first demonstrated in a lensless setup in 2004 [1], is a rather novel approach that is still under heavy development and significant improvements have been made in the past few years [2–12]. Still, permanent holography end stations with user support, as common for more established techniques such as (scanning) transmission X-ray microscopy (STXM) or photo emission electron microscopy (PEEM), are not yet available. Therefore, the following chapter discusses the key ingredients and solutions for the main challenges of X-ray holography from an end user perspective. Specifically, the content of this chapter is organized as follows: The basic theory of how to obtain a hologram and how to reconstruct the real space information is presented in Section 2; the tricks of time resolved measurements and how to measure time zero in Section 3; some of the most important considerations for efficient imaging in Section 4; a suggested end station for magnetic imaging in Section 5; steps of how to fabricate suitable samples in Section 6; and finally, an outlook of anticipated future developments in Section 7. For those interested in more fundamental and technical aspects of X-ray holography, I suggest the other specialized literature, for example [9, 13].

2. How to obtain a real space image

A typical and convenient realization of X-ray holography is in a lensless off-axis geometry as depicted in **Figure 1**. Here, the entire optics of the imaging process constitutes of a mask in the X-ray beam with two circular apertures, the so-called object and reference holes. The object hole is typically approximately 1 μm in diameter and the reference hole is roughly 50 nm in diameter. The two holes are separated by 2–5 μm (at least three times the object hole radius) in the direction transverse to the incident beam. The specimen that is to be imaged is placed behind the object hole, ideally rigidly attached to the mask to exclude drift of the reconstructed image. The beam is transmitted through both holes and the specimen and is diffracted due to absorption and phase modulation during the transmission process. The hologram, that is, the interference pattern of the two diffracted beams, is recorded using a camera. For details regarding the wave propagation, see Refs. [9, 13]. Here, we consider the typical application where the camera is placed in the far field of the scattering process. Therefore, the scattering amplitude is conveniently described by the Fourier transform of the total transmission function of sample and mask.

The camera detects the intensity of the scattered light. Mathematically, the intensity is the absolute square of the scattering amplitude. An inverse Fourier transform of this intensity pattern yields the so-called reconstruction, which is the autocorrelation of the original total transmission function. The reconstruction can be written as a sum of the autocorrelations of object hole transmission function and reference hole transmission function plus the cross-correlations between these two transmission functions. When pictured, the autocorrelation is located in the center of the reconstruction and the cross-correlation terms are displaced by the vector from object hole to reference and vice versa, see **Figure 1**. Hence, there is no

spatial overlap between these terms. Since the reference is small, the cross-correlation yields an image of the transmission function of the specimen with a resolution determined mainly by the reference hole diameter [1, 13].

In theory, reconstructing the real space image of a specimen from a hologram is just a simple Fourier transform. However, in practice, a number of post-processing steps are required to obtain a high quality image, as briefly discussed subsequently. First, a hologram is seldom recorded without artifacts. For instance, cosmic rays, stray light, pixel defects, and particles on the camera chip lead to overly bright or dark pixels in the hologram and to wave-like noise in the reconstruction. Such artifacts can be eliminated by statistical analysis (e.g., identifying artifacts as pixels deviating from the local average intensity by many standard deviations and by much more than a single photon count) and by subtracting a dark image. Other artificial artifacts, such as a central beam stop and the wire holding it, can be smoothed to avoid high intensity noise in the reconstruction due to sharp edges in the hologram. Best results are obtained when using high quality camera chips (typically 2048×2048 pixels) with a low noise readout electronics and by carefully eliminating sources of stray light.
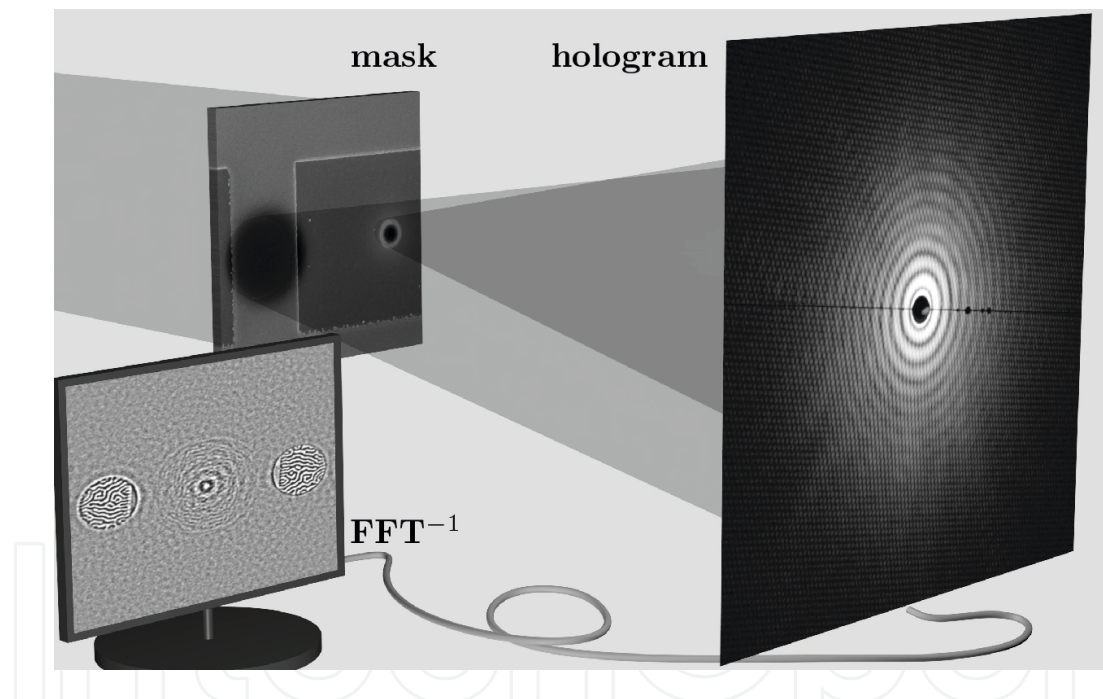

Figure 1. Schematic illustration of X-ray holography. The sample (labeled mask) is illuminated with a coherent plane wave from the left. The sample consists of a transparent SiN membrane. On the back side is an opaque Au layer with two holes, a larger one (the object hole, typically 1 μm in diameter and a smaller one (the reference hole, typically 50 nm in diameter). These holes are visible as dark shadows in the scanning electron micrograph overlaid on the mask. On the front side of the SiN membrane is the specimen that is to be imaged: In the present example, a magnetic film patterned into a wire. The incident beam is transmitted through the two holes and gets scattered. In the far field, the interference of the two scattered beams forms the hologram, which is recorded with a camera. The direct beam is blocked via a circular beam stop (typically made by a drop of glue on a thin wire, both of which are visible as a black circle and a black line in the hologram) so that the dynamic range of the camera can be optimized to detect the diffracted beam. The hologram can be digitally reconstructed via an inverse Fourier transform FFT $^{-1}$ to obtain the local transmission function of the sample, here showing the out-of-plane magnetization of the sample as black and white contrast. The image of the sample appears twice, a phenomenon known as twin image formation.

In a second step, the center of the hologram has to be found. This will be the center for the Fourier transform. At least one pixel precision should be aimed for to avoid strong wavy modulations of the reconstruction. However, by Fourier identities, a displacement in the hologram is equivalent to a phase shift in the reconstruction. Therefore, centering can also be performed in the reconstruction by multiplication with a plane wave $exp^{(i(k_x x + k_y y))}$, where x and y are coordinates in the reconstruction and k_x and k_y measure the center displacement in the hologram, both in pixels. With this method, sub-pixel centering can be achieved.

The third manipulation of the hologram is a numerical correction for the fact that specimen and reference typically have a finite relative shift in the propagation direction of the beam. In **Figure 1**, the reference exit wave is formed approximately 1 μm upstream of the specimen due to the finite thickness of mask, SiN membrane, and the specimen itself. Also, the reference itself acts as a focusing optics, introducing another in-line displacement between the smallest spot of the reference beam (i.e., the best resolution for the reconstruction) and the specimen [14]. The hologram contains the full wave field information (intensity and phase). Therefore, the reference focus can be numerically moved along the beam direction until both reference focus and specimen are in a common plane perpendicular to the beam [6]. Using this reference propagation algorithm often significantly improves the reconstruction quality and resolution and allows to obtain depth information of three dimensional specimen [4].

Strictly speaking, the hologram is the Fourier transform of the transmission function only if measured on a spherical detector. In practice, however, detectors are planar. For very close camera distances, an inverse gnomonic projection of the hologram is required to correct for this geometrical artifact [15]. In our measurements, such a correction has only been required if scattering angles exceeding 5° were recorded.

The reconstruction is in general complex valued. In theory, real and imaginary part of the reconstruction measure the refracting and absorptive part of the refractive index of the specimen, respectively [16]. However, such a quantitative correlation requires excellent centering, patching of the intensity blocked by the beam stop, a very low noise hologram, and a homogeneous phase across the reference beam. In most applications, it is therefore more practical to artificially shift all the relevant information into the real part by multiplying a constant phase factor to the reconstruction. The real part can subsequently be displayed as an image.

With an optimized sample design (see Section 4) and after following the previously described reconstruction steps, a high quality reconstruction of a magnetic sample as shown in **Figure 1** can be obtained from two camera accumulations (each with a maximum of 1500 photons per pixel), one for left-circular polarized light and one for right-circular polarized light. The total acquisition time, excluding camera readout and polarization change, can be as low as 1 s at a high intensity, high coherence beamline such as P04 at PETRA III in Hamburg, Germany.

3. Time-resolved measurements

In general, there are two ways of time-resolved imaging: The first way is single-shot imaging, where images are acquired on a time scale much shorter than the dynamics that is to be observed. Here, the dynamics is recorded as it is happening, without any need of

reproducibility. However, when temporal resolution in the nanosecond regime or below and simultaneous spatial resolution in the nanometer regime is needed, the intensity of the light required to obtain a single image becomes so large that the sample evaporates on a picosecond time scale. X-ray holography is unique in being capable of recording single shot videos with only a few femtoseconds between the frames [17], that is, before the atoms of the sample start to move, but the approach is limited to a few frames and to sub-picosecond imaging.

For longer time scales or more frames, pump-probe imaging needs to be employed. Here, the intensity in a single shot is so low that the sample remains unperturbed. However, in order to obtain an image, many such shots need to be accumulated and the sample needs to be in an identical state during every shot. Besides a perfect reproducibility of the dynamics in the specimen, two steps are critical to enable such a pump-probe experiment: First, the excitation that triggers the dynamics must be periodic with a repetition that exactly matches the repetition rate of the incident photon pulses. And second, it is crucial to know the time at which the excitation should be applied in order to arrive simultaneously with the photons at the sample. Details of how to realize this precise timing are discussed in the appendix.

Once the excitation is in sync with the probing X-rays, images can be acquired at every delay of interest between pump and probe. That is, videos are recorded in a frame-by-frame mode: The delay between pump and probe is fixed for one image. After the acquisition of each image, the delay is changed and the accumulation of a new frame starts.

4. Efficient imaging

There are a great number of parameters that can be tweaked in X-ray holography in order to optimize the imaging for the specific scientific question. These parameters include the following: (i) object hole diameter; (ii) reference hole diameter; (iii) distance between object hole and reference hole; (iv) contrast of the specimen (e.g., thickness of a magnetic material); (v) camera-specimen distance; (vi) number of pixels of the camera and pixel size (changed by, e.g., binning and region of interest); (viii) camera gain or sensitivity; (ix) beam stop diameter; (x) an absorptive layer in or before the specimen (a parameter that is called here object linear transmission); and many more. Optimizing these parameters can yield orders of magnitude better contrast in the reconstructed image, and it is strongly recommended to use simulations to determine the optimum parameters.

Figure 2 illustrates how the contrast of a magnetic stripe domain image depends on some of the aforementioned parameters. The reconstructions were obtained from simulations of a purely two dimensional sample with a circular reference and a Co-containing magnetic specimen in a stripe domain phase. Contrast is generated exploiting the X-ray magnetic circular dichroism of the Co magnetic domains, that is, in absorption lengths of 13.7 nm for up domains and 23.4 nm for down domains [18]. For the simulations, the specimen is modeled as a magnetic layer with a total Co thickness of 2 nm, a hexagonal lattice of 125-nm diameter bubble domains, and a object linear transmission of 25%. The object hole has a diameter of 1.5 μm, the reference hole a diameter of 50 nm, and the distance between the two is fixed to 4 μm. The camera is a chip of 2048 × 2048 pixels of 13.5 × 13.5 μm² size at a distance of 24 cm to the sample. The sensitivity is assumed to be 50 counts per photon and the readout noise

is 3 counts per pixel in average. The camera saturates at 64,000 counts. The model includes a beam stop of 1 mm diameter, a coherence of 80.00% and sample vibrations relative to the camera of 300 nm.

The simulations in **Figure 2** demonstrate how significantly the contrast is determined by the intensity ratio of object and reference, the overall coherence, and the dynamic range of the camera. Within a reasonable range and assuming that the intensity of the incoming flux is not a limiting factor, more absorption of the object and a smaller object hole improve the intensity ratio of reference to object and yield better contrast. That is, the image quality can be improved by coating the specimen with some absorptive layer.
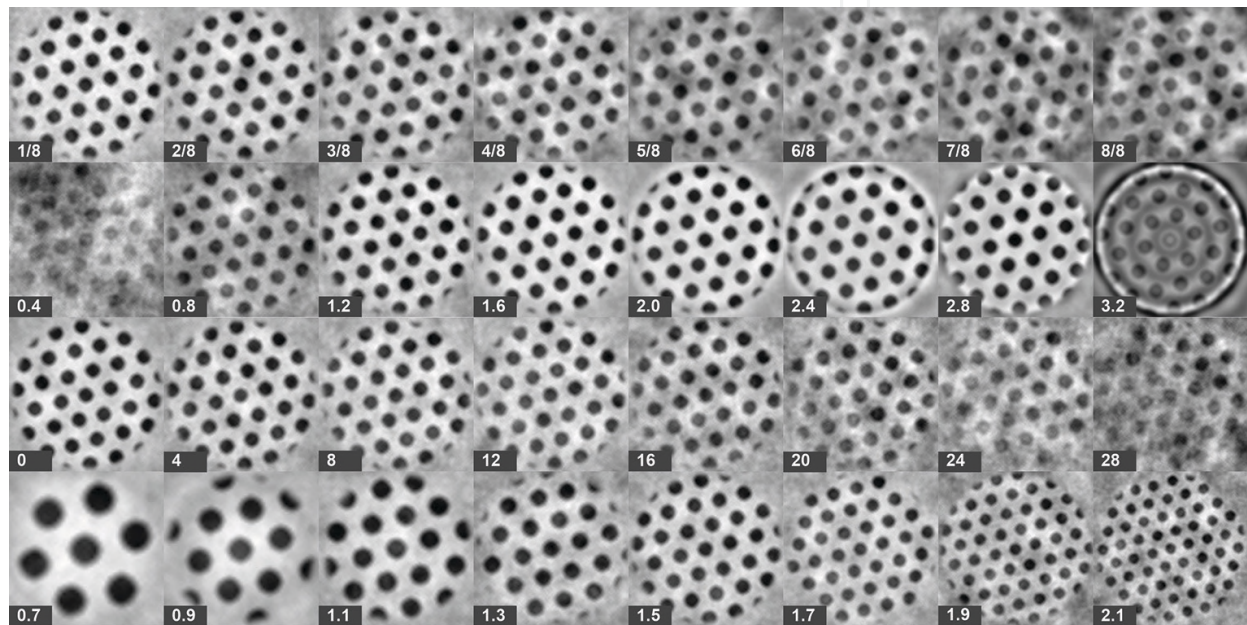

Figure 2. Contrast of the reconstruction as a function of imaging parameters. Top row: Object linear transmission, from 0.125 (left) to 1.0 (right) in steps of 0.125. Second row: Beamstop diameter, from 0.4 mm (left) to 3.2 mm (right) in steps of 0.4 mm. Third row: Vibrations (sigma of a Gaussian distribution), from 0 (left) to 28 µm (right) in steps of 4 m. Bottom row: Object hole size, from 700 nm (left) to 2100 nm (right) in steps of 200 nm.

The presence of a beam stop allows for using the dynamic range of the camera to detect signals at high scattering angles, which generally increases the contrast. However, if the beam stop becomes too large, the missing small scattering angle signals (corresponding to constant or low frequency modulations in the hologram) offset the intensity level of the reconstruction. The effect can be seen in **Figure 2** for a beam stop diameter of 2.4 mm. The white domains have now a color comparable to the background. For an even larger beam stop, the effect of ringing can be observed, as illustrated for the 3.2 mm beam stop. The optimum size of the beam stop depends on most of the other imaging parameters and has to be determined from simulations.

Finally, vibrations between the sample and the camera have a similar effect as a reduced coherence of the incoming beam [19]: Speckles and interference modulations become blurred and the image contrast reduces. Similar to the beam stop size, the question of at which magnitude

the vibrations negatively effect the contrast can be answered only through simulations. In the present case, vibrations of as much as 8 μm have almost no effect on the image quality. However, for other geometries, the threshold may be as low as 300 nm.

Experimentally, the following parameters have been verified to yield full black-white contrast of magnetic domains in a single camera acquisition per helicity and a spatial resolution of better than 20 nm: (almost) fully coherent photons with energy at the Co L_3 edge (778 eV); an object hole with 800 nm field of view; a 50 nm reference that has its most constricted part on the camera side of the mask (considering that most references are conical); a center-to-center distance of 3 μm between object and reference holes; a specimen with a total of 9 nm of Co and a nonmagnetic absorption of 75%; a camera with 2048 × 2048 pixels of 13.5 μm size at a distance of 17 cm to the sample operated using 1 MHz low noise readout; a beam stop diameter of 0.75 mm diameter blocking just the central part of the object hole's airy disk; and a rigid mounting of the sample and the camera. The relatively small size of the object hole and the absorptive layer lead to a favorable total intensity ratio of object and reference beams, which manifests in a clear interference modulation of the entire hologram, including the center, as visible in **Figure 1**. Fine speckle patterns can be distinguished in the hologram due to the good coherence and the reduction in relative transverse vibrations between camera and sample. The excellent resolution is obtained due to a focus formed by a cylindrical reference in a thick mask material [14] and the large numerical aperture associated with a close camera distance.

5. Experimental setup

The design of a holographic end station should be tailored to the actual scientific question of the experiment. In contrast to many other imaging techniques, holography gives the user a large flexibility for instrumentation in the vicinity of the sample. Because of the absence of optical elements, an area of typically 20 cm radius around the sample is freely available and can be used to apply electromagnetic fields or temperature to the sample. Even optical excitations are possible when using a filter of, e.g., aluminum to shield the camera from this form of stray light. To reduce the effect of vibrations, it is recommended to mount the sample on a rigid holder and fix it onto the vacuum chamber.

Figure 3 illustrates an example of a chamber optimized for magnetic imaging. The beam first passes through a 1 mm aperture to facilitate a vacuum pressure gradient of two orders of magnitude between the two sides of the aperture. This way the chamber can be operated in pressures of as high as 5×10^{-6} mbar, thus avoiding restrictions to ultra high vacuum components and enabling quick venting and pumping. Carbon deposition on the sample was found to be negligible, even when imaging a single sample for more than one week in such a poor vacuum, at least when using photon energies exceeding 700 eV. The suggested chamber has a quadrupole magnet that can produce fields of larger than 1T at a gap of 2 mm, a shutter to stop the illumination during camera readout, a camera with a beam stop, and a sample held by a rigid mounting.
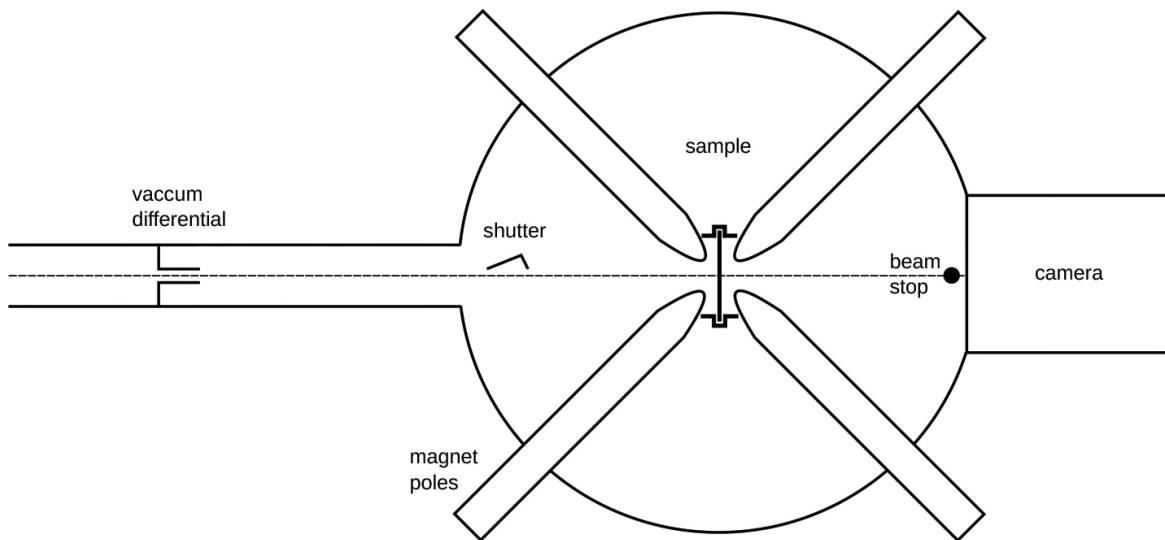
Figure 3. Top-view schematic of a holographic imaging chamber.

6. Sample fabrication

In the conventional approach, X-ray holography samples are integrated with the holographic masks, leading to the unique advantage of inherently drift-free imaging at the price of exceptionally complex sample fabrication. There is a concept to separate mask and specimen [2, 3], but it requires giving up drift-free imaging and hence the main argument for using X-ray holography instead of, e.g., STXM. Therefore, in the foreseeable future, the fabrication of advanced integrated samples will remain one of the main challenges of X-ray holography from an end users perspective. A detailed recipe has been published in [10], which will be briefly reviewed here.

Despite some demonstration of X-ray holography in reflection geometry [8], most present day applications of the technique rely on transmission measurements of transparent samples. Soft X-rays have a sub-micrometer penetration depth in any solid material. Hence, free standing films, the so-called membranes, are required to support the specimen, which itself needs to be thin. The most wide-spread approach is to use commercially available silicon nitride (SiN) membranes. The thickness of the membrane needs to be adapted to the specific imaging conditions, in particular to the photon energy. For instance, for magnetic imaging at the transition metal M edges (around 60 eV), anything more than a few tens of nanometers would already be opaque. For measurements at energies exceeding 500 eV, thicknesses of 500 nm and more are feasible and often even advisable because of the increased stability and robustness against various fabrication hardships. For the same reason, membranes should not be unnecessarily large, that is, their size should be just enough to fit the object and reference holes.

Figure 4 illustrates the steps to fabricate a sophisticated sample that is suitable for time-resolved imaging of field-induced magnetic domain dynamics [10, 20]. Not all of these steps are required for every sample. However, all holographic samples start with a membrane (step a) with an opaque layer on the back side (step b). $[Cr(5)/Au(55)]_{20}$ has proven suitable for imaging at 778 eV, where the transmission of this stack is below 10^{-9}. The absorption is mainly

due to the gold. The chrome layers prevent the formation of large Au grains, which significantly eases focused ion beam (FIB) milling of the material. Steps c, g, and h, that is, FIB milling of the object and reference holes, are also required in any holography sample process. In principle, any process can be used to prepare a specimen on the front side of the membrane as long as ultrasonic exposure is avoided. In **Figure 4**, the remaining steps are marker fabrication (step d), material deposition and shaping (step e), and patterning of a microcoil (step f).
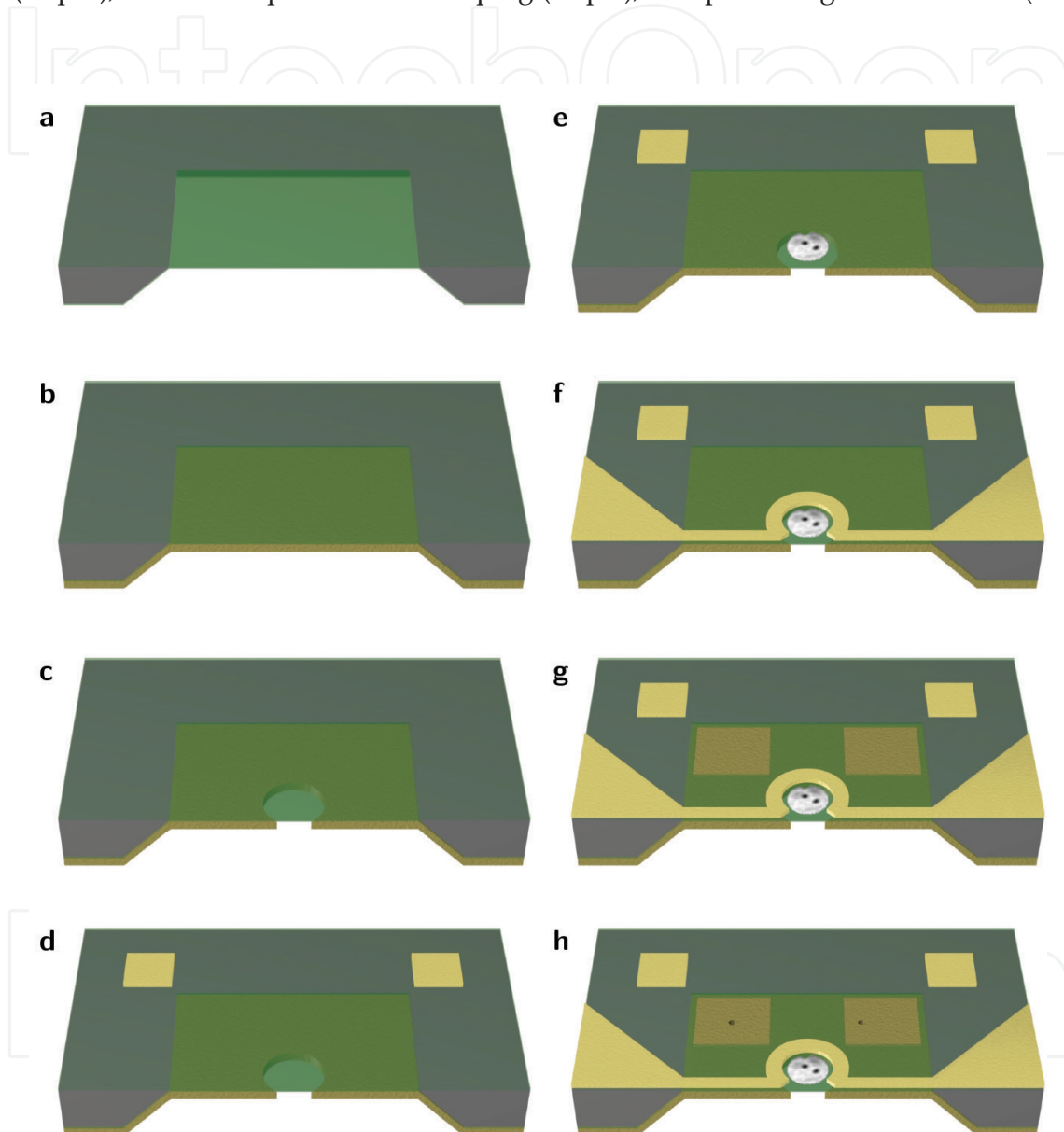

Figure 4. Steps for fabrication of a holographic sample. (a) Starting with a commercially available SiN membrane of a few micro meters in lateral dimensions. (b) An opaque Cr/Au multilayer is deposited on the topographic side of the membrane. (c) The Cr/Au is removed in a circular region, defining the object hole. The SiN is not removed. (d) Alignment markers are fabricated to align subsequent steps with respect to the object hole. (e) A disk-shaped magnetic specimen is fabricated behind the object hole. (f) A microcoil is wrapped tightly around the magnetic specimen to generate short magnetic field pulses. (g) The SiN is removed in large squarish areas where the references are supposed to be located. The removal of SiN makes the fabrication of small references significantly easier. (h) References are prepared in the previously designated areas. Reproduced from Ref. [10].

The result of this process can be seen in **Figure 5**. Note that optical lithography or even simple shadow-masking can be used to considerably simplify the overall process if sub-micrometer alignment precision is not required.
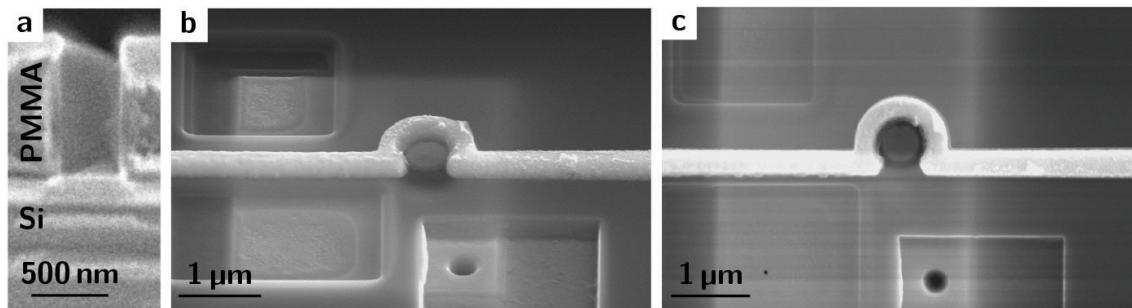

Figure 5. Scanning electron micrographs of a holographic sample. (a) Cross section of the PMMA resist used to fabricate the microcoil. Steep walls are required to prepare the coil in close vicinity to the magnetic specimen. (b) View of the final sample under 52°. The disk-shaped element in the center is the magnetic specimen. The black halo around it is the object hole visible through the SiN membrane. Wrapped around the sample is a gold microcoil. Three large square pads are milled into the SiN membrane to facilitate the fabrication of reference holes. One of the reference holes was milled from this side of the sample, here visible as a large conical aperture. (c) Top view of the same sample, now also showing the second reference in the bottom-left pad. This reference was milled from the other side of the sample and the exit is much more constricted then the entrance. The properties of the reference wave depend significant on whether the beam first passes the conical part or first the constricted part [14]. Reproduced from [10].

7. Outlook

So far, most reports using X-ray holography are improving the technique itself. Only a few studies exist where X-ray holography has been used to answer a scientific question not related to optics or imaging, and most of those where published in collaboration with the same groups that developed the technique (e.g. [20–26]). It is still a long way before X-ray holography will be a standard imaging tool, available to a similarly large community as STXM or PEEM. Above all, permanent end stations with full user support are needed. The new soft X-ray synchotron MAX IV in Lund, Sweden, will probably be the first to provide such an end station. However, even now, imaging times and quality are at least competitive to other soft X-ray imaging techniques and the parameters to achieve such performance have been discussed in this chapter. The perspective of improved cameras with readout times of sub-milliseconds (compared to the present 4 s) and single pixel adjustable gain in concert with even higher X-ray intensities and fast helicity switches suggest that almost live imaging will be possible in the future.

Acknowledgements

Appendix

Here, we discuss the electronics to realize time-resolved X-ray holographic imaging using the example of electrical excitations and imaging in the 1.25 MHz repetition rate single bunch mode of BESSY II in Berlin, Germany [20, 27, 28]. The following discussion is largely adapted from Ref. [28].
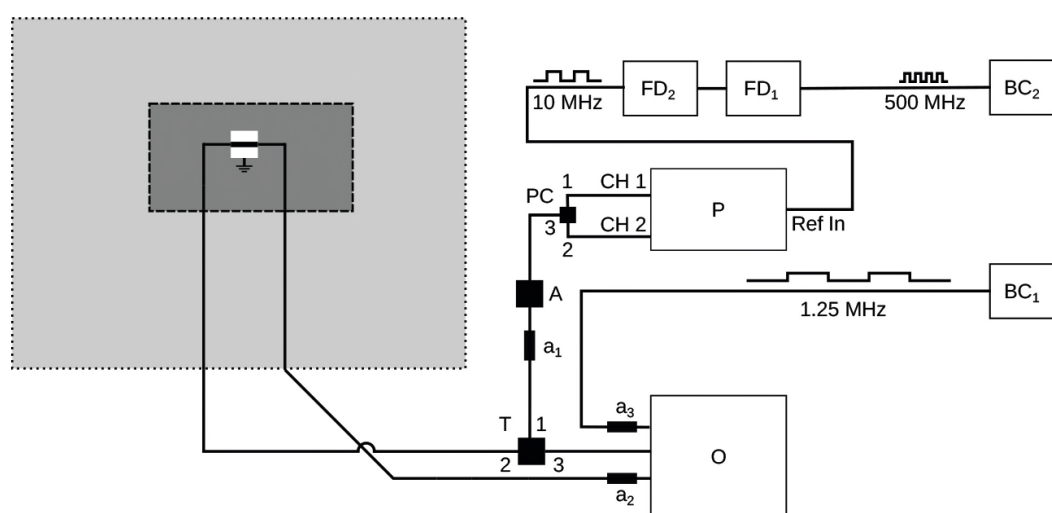

Figure 6. Electrical schematics for pump-probe X-ray holography. The outer light gray rectangle symbolizes the vacuum chamber and the inner dark gray rectangle the sample board. The sample itself is depicted as a white square with a horizontal wire on top. The thick black lines denote high frequency cables with SMA connectors. The acronyms represent the following: *a* stands for attenuator, *T* for pick-off tee, *A* for amplifier, *O* for oscilloscope, *P* for pulse generator, *PC* for power combiner, *CH* for channel, *FD* for frequency divider, and *BC* for bunch clock. A more detailed discussion of the figure is provided in the text. Reproduced from Ref. [28].

A schematic of the electrical circuit for the synchronized pulse injection is drawn in **Figure 6**. We use a Picosecond Pulse Labs 12080 800 MHz pulse generator (P in **Figure 6**) that has two individually programmable output channels, each with two SMA-type output connectors: one for the normal and one for the inverted signal. Each channel can create rectangular pulses with sub-100 ps rise time with up to 2 V bipolar amplitude and up to 800 MHz repetition rate. Both outputs provide adjustable time delays. The pulse generator has an internal 10 MHz clock, which can be replaced by an external clock signal (at Ref In). To ensure that the pulse generator injects pulses with the same repetition rate as that of the incident photon pulses (which is slightly less than 1.25 MHz in the single bunch mode of BESSY II), the eightfold multiple of the synchrotron pulse repetition rate (which is slightly <10 MHz) is fed into the pulse

generator as a 10 MHz clock signal. With respect to this external clock, a 1.25 MHz signal has the exact same repetition rate as the photon pulses.

To create such a 10 MHz signal from the synchrotron, we use the 400-fold single bunch frequency (approximately 500 MHz), because such a signal is provided by the synchrotron (at bunch clock BC_2) and because it is much easier to reduce the frequency of a signal than multiplying it. That is, we use frequency dividers (FD_1 and FD_2 in **Figure 6**), where the first one (FD_1) divides the frequency by 25, and the second one (FD_2) divides by another factor 2%. The reason for not using directly a division factor of 50% is that this would result in a rectangular pulse pattern with a duty cycle of 2 (1/50), whereas our setup with two frequency dividers provides the 50 duty cycle signal expected by the pulse generator.

We can use this pulse generator to create bipolar rectangular pulses with variable amplitudes in both polarities. For this purpose, we use channel 1 (CH 1) of the pulse generator for the positive pulse and the inverted channel two ($\overline{\text{CH2}}$) for the negative pulse. The relative delay between the pulses is set to the duration of the first pulse, thus creating an uninterrupted succession of both pulse polarities, which is often useful because this pulse shape provides the strongest change of excitation at a given ohmic heat load. The signal from both outputs is combined using a power combiner (PC) that combines the input signals on connectors 1 and 2 in the output connector 3. The combined signal is amplified by 32 dB (power gain factor of 1600, voltage increase by a factor of 40) using a built-to-order Kuhne KU PA BB 5030 A amplifier (A) with a band width of 10–1500 MHz. To protect the amplifier against reflected signals, an attenuator of −3 dB (a_1) is mounted at its output. Any reflection will pass the attenuator twice and will thus be attenuated by −6 dB.
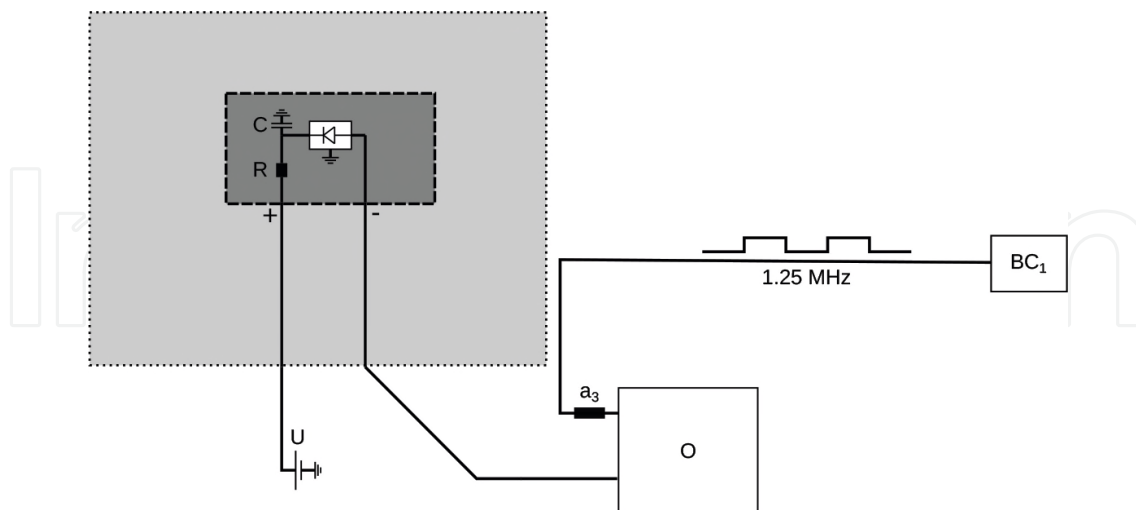

Figure 7. Electrical schematics for the time zero determination with an APD. The outer light gray rectangle symbolizes the vacuum chamber and the inner dark gray rectangle the APD board. The APD itself is depicted as a white diode symbol on the APD board. On the positive contact side of the APD, a 1 MΩ resistor R and a 1nF capacitor C are integrated in the APD board. A source meter is used to supply a voltage of 100 V on the positive input of the APD. The negative side is connected with cables of well-known length with the oscilloscope O. This oscilloscope is triggered by the 1.25 MHz bunch clock signal BC_1 provided by the synchrotron. Reproduced from [28].

Before being injected into the sample, part of the amplified signal is picked off to be monitored with a LeCroy WavePro 735ZI 3.5 GHz real time oscilloscope (O). This splitting of the signal is performed using a built-to-order Kuhne KU DIV 0112 A—371 pick-off tee (T), which splits the input signal on connector 1 in two parts, one almost unperturbed (power reduced by −2 dB) on output 2 and the other one attenuated by −20 dB on output 3. The signal from output 3 is monitored on the oscilloscope, whereas the signal from output 2 is injected into a microcoil on the sample, creating a magnetic field pulse (for details of the sample geometry, see **Figures 4** and **5**). Part of the pulse is transmitted and subsequently recorded with the oscilloscope (optionally attenuated at a_2), another part is absorbed by heating the microcoil, and the rest is reflected and sent through the pick-off tee again with −20 dB attenuation to the oscilloscope. The current transmitted through the microcoil can be calculated from the voltage of the transmitted signal recorded on the oscilloscope (if present, corrected by the damping of a_2) divided by its 50 Ω input impedance.

We now send bipolar pulses with a repetition rate synchronized to the incident photon pulses through the microcoil. The remaining challenge is to have both pulses simultaneously on the sample. For this purpose, we use the rising edge of the 1.25 MHz bunch clock signal (BC_1) provided by the synchrotron as a reference time zero, that is, we record this bunch clock signal on the oscilloscope (attenuated by −20 dB (at a_3) because its voltage is too large for the oscilloscope) and set its trigger to the respective channel. The temporal position of the photon pulse with respect to the same trigger is determined by mounting a Hamamatsu S9717-05K fast Avalanche Photo Diode (APD) on the position at which the sample is during the measurement, and using cables to transport the signal from the APD to the oscilloscope of precisely the same length as in the excitation scheme. The circuit used for this measurement is sketched in **Figure 7**. One side of the APD is connected to the oscilloscope, which is triggered by the BC_1 bunch clock signal. That is, this side is electrically on ground potential. The other side is lifted
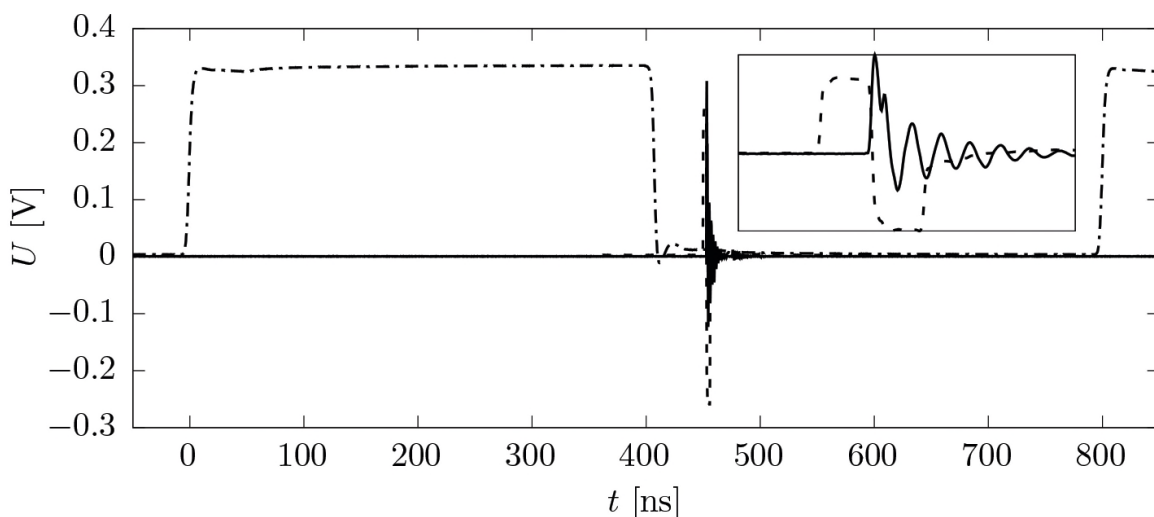

Figure 8. Signal measured with the oscilloscope. The dash-dotted line is the bunch clock BC_1 that serves as a trigger for the oscilloscope. The 50% level of the rising edge of this signal defines the time zero of the oscilloscope. The solid line is the signal from the APD (multiplied by 5), and the dashed line is the transmitted pulse (divided by 10). The latter two signals are plotted enlarged in the inset. Reproduced from Ref. [28].

to 100 V, and part of this potential drops on a 1 MΩ resistor placed in series before the APD. In this configuration, the diode is operated in reverse bias mode, that is, the depletion zone is increased by the electric field gradient. The resistance of the diode is much larger than 1 MΩ, such that almost the whole 100 V drop at the APD. A 1nF capacitor couples this side of the APD to ground; in the static case, however, this capacitor is insulating. As soon as a photon is absorbed in the diode, the situation changes significantly. The photons create free electrons that are accelerated in the external potential and create an avalanche of new charge carriers by collisions during their motion (hence the name APD). The capacitor acts as a sink for the (temporarily) generated charges. The holes are filled by a current from the oscilloscope, which is detected as a positive voltage peak. The avalanche stops because the voltage at the APD decreases immediately as the device becomes conducting (then most of the voltage drops at the 1 MΩ resistor). The signal decays in oscillations characteristic of the complicated RLC equivalent internal circuit of the diode [29]. The time of the photon event is reconstructed from the start of the pulse on the oscilloscope.

The signal recorded with the oscilloscope is plotted in **Figure 8**. The dash-dotted line depicts the 1.25 MHz bunch clock signal BC_1. The 50.00% level of its rising edge defines the time zero of the oscilloscope. The photon pulse found on the APD (solid line) starts at $t=452.7$ ns with respect to the oscilloscope trigger. After changing to the sample setup, the pulse send through the sample (dashed line) arrives at the same time delay at the oscilloscope. In this example, the magnetic state is probed at the transition between positive and negative pulse.

Author details

Felix Büttner

Address all correspondence to: felixbuttner@gmail.com

Department of Materials Science and Engineering, Massachusetts Institute of Technology, Cambridge, MA, USA

References

[1] Eisebitt S, Lüning J, Schlotter WF, Lorgen M, Hellwig O, Eberhardt W, Stöhr J. Lensless imaging of magnetic nanostructures by X-ray spectro-holography. Nature. 2004;**432**:885–888. doi:10.1038/nature03139

[2] Tieg C, Frömter R, Stickler D, Stillrich H, Menk C, Streit-Nierobisch S, Stadler LM, Gutt C, Leupold O, Sprung M, Grübel G, Oepen HP. Overcoming the field-of-view restrictions in soft x-ray holographic imaging. Journal of Physics: Conference Series. 2010;**211**:012024. doi:10.1088/1742-6596/211/1/012024

[3] Stickler D, Frömter R, Stillrich H, Menk C, Tieg C, Streit-Nierobisch S, Sprung M, Gutt C, Stadler LM, Leupold O, Grübel G, Oepen HP. Soft x-ray holographic microscopy. Applied Physics Letters. 2010;**96**:042501. doi:10.1063/1.3291942

[4]   Geilhufe J, Tieg C, Pfau B, Günther CM, Guehrs E, Schaffert S, Eisebitt S. Extracting depth information of 3-dimensional structures from a single-view X-ray Fourier-transform hologram. Optics Express. 2014;**22**:24959–24969. doi:10.1364/OE.22.024959

[5]   Geilhufe J, Pfau B, Schneider M, Büttner F, Günther CM, Werner S, Schaffert S, Guehrs E, Frömmel S, Kläui M, Eisebitt S. Monolithic focused reference beam X-ray holography. Nature Communications. 2014;**5**:3008. doi:10.1038/ncomms4008

[6]   Guehrs E, Günther CM, Pfau B, Rander T, Schaffert S, Schlotter WF, Eisebitt S. Wavefield back-propagation in high-resolution X-ray holography with a movable field of view. Optics Express. 2010;**18**:18922–18931. doi:10.1364/OE.18.018922

[7]   Martin AV, D'Alfonso AJ, Wang F, Bean R, Capotondi F, Kirian RA, Pedersoli E, Raimondi L, Stellato F, Yoon CH, Chapman HN. X-ray holography with a customizable reference. Nature Communications. 2014;**5**:4661. doi:10.1038/ncomms5661

[8]   Roy S, Parks D, Seu KA, Su R, Turner JJ, Chao W, Anderson EH, Cabrini S, Kevan SD. Lensless X-ray imaging in reflection geometry. Nature Photonics. 2011;**5**:243–245. doi:10.1038/nphoton.2011.11

[9]   Pfau B, Günther CM, Schaffert S, Mitzner R, Siemer B, Roling S, Zacharias H, Kutz O, Rudolph I, Treusch R, Eisebitt S. Femtosecond pulse x-ray imaging with a large field of view. New Journal of Physics. 2010;**12**:095006. doi:10.1088/1367-2630/12/9/095006

[10] Büttner F, Schneider M, Günther CM, Vaz CAF, Lägel B, Berger D, Selve S, Kläui M, Eisebitt S. Automatable sample fabrication process for pump-probe X-ray holographic imaging. Optics Express. 2013;**21**:30563–30572. doi:10.1364/OE.21.030563

[11] Duckworth TA, Ogrin FY, Beutier G, Dhesi SS, Cavill SA, Langridge S, Whiteside A, Moore T, Dupraz M, Yakhou F, van der Laan G. Holographic imaging of interlayer coupling in Co/Pt/NiFe. New Journal of Physics. 2013;**15**:023045. doi:10.1088/1367-2630/15/2/023045

[12] Duckworth TA, Ogrin F, Dhesi SS, Langridge S, Whiteside A, Moore T, Beutier G, van der Laan G. Magnetic imaging by x-ray holography using extended references. Optics Express. 2011;**19**:16223. doi:10.1364/OE.19.016223

[13] Pfau B, Eisebitt S. X-Ray Holography. In: Jaeschke EJ, Khan S, Schneider JR, Hastings JB, editors. Synchrotron Light Sources and Free-Electron Lasers. Cham: Springer International Publishing. 2016; p. 1093–1133.

[14] Geilhufe J. High resolution soft X-ray Fourier transform holography [thesis]. Berlin: TU Berlin; 2015.

[15] Schaffert S, Pfau B, Geilhufe J, Günther CM, Schneider M, von Korff Schmising C, Eisebitt S. High-resolution magnetic-domain imaging by Fourier transform holography at 21 nm wavelength. New Journal of Physics. 2013;**15**:093042. doi:10.1088/1367-2630/15/9/093042

[16] Scherz A, Schlotter WF, Chen K, Rick R, Stöhr J, Lüning J, McNulty I, Günther CM, Radu F, Eberhardt W, Hellwig O, Eisebitt S. Phase imaging of magnetic nanostructures

using resonant soft x-ray holography. Physical Review B. 2007;**76**:214410. doi:10.1103/PhysRevB.76.214410

[17]   Günther CM, Pfau B, Mitzner R, Siemer B, Roling S, Zacharias H, Kutz O, Rudolph I, Schondelmaier D, Treusch R, Eisebitt S. Sequential femtosecond X-ray imaging. Nature Photonics. 2011;**5**:99–102. doi:10.1038/nphoton.2010.287

[18]   Stöhr J, Siegmann HC. Magnetism—From Fundamentals to Nanoscale Dynamics. Berlin, Heidelberg: Springer-Verlag; 2006.

[19]   Thibault P, Menzel A. Reconstructing state mixtures from diffraction measurements. Nature. 2013;**494**:68–71. doi:10.1038/nature11806

[20]   Büttner F, Moutafis C, Schneider M, Krüger B, Günther CM, Geilhufe J, von Korff Schmising C, Mohanty J, Pfau B, Schaffert S, Bisig A, Foerster M, Schulz T, Vaz CAF, Franken JH, Swagten HJM, Kläui M, Eisebitt S. Dynamics and inertia of skyrmionic spin structures. Nature Physics. 2015;**11**:225–228. doi:10.1038/nphys3234

[21]   Wang T, Zhu D, Wu B, Graves C, Schaffert S, Rander T, Müller L, Vodungbo B, Baumier C, Bernstein DP, Bräuer B, Cros V, de Jong S, Delaunay R, Fognini A, Kukreja R, Lee S, López-Flores V, Mohanty J, Pfau B, Popescu H, Sacchi M, Sardinha AB, Sirotti F, Zeitoun P, Messerschmidt M, Turner JJ, Schlotter WF, Hellwig O, Mattana R, Jaouen N, Fortuna F, Acremann Y, Gutt C, Dürr HA, Beaurepaire E, Boeglin C, Eisebitt S, Grübel G, Lüning J, Stöhr J, Scherz AO. Femtosecond single-shot imaging of nanoscale ferromagnetic order in Co/Pd multilayers using resonant x-Ray holography. Physical Review Letters. 2012;**108**:267403. doi:10.1103/PhysRevLett.108.267403

[22]   Günther CM, Hellwig O, Menzel A, Pfau B, Radu F, Makarov D, Albrecht M, Goncharov A, Schrefl T, Schlotter WF, Rick R, Lüning J, Eisebitt S. Microscopic reversal behavior of magnetically capped nanospheres. Physical Review B. 2010;**81**:064411. doi:10.1103/PhysRevB.81.064411

[23]   Hauet T, Günther CM, Pfau B, Schabes ME, Thiele JU, Rick RL, Fischer P, Eisebitt S, Hellwig O. Direct observation of field and temperature induced domain replication in dipolar coupled perpendicular anisotropy films. Physical Review B. 2008;**77**:184421. doi:10.1103/PhysRevB.77.184421

[24]   Pfau B, Günther CM, Guehrs E, Hauet T, Hennen T, Eisebitt S, Hellwig O. Influence of stray fields on the switching-field distribution for bit-patterned media based on pre-patterned substrates. Applied Physics Letters. 2014;**105**:132407. doi:10.1063/1.4896982

[25]   Pfau B, Günther CM, Guehrs E, Hauet T, Yang H, Vinh L, Xu X, Yaney D, Rick R, Eisebitt S, Hellwig O. Origin of magnetic switching field distribution in bit patterned media based on pre-patterned substrates. Applied Physics Letters. 2011;**99**:062502. doi:10.1063/1.3623488

[26]   von Korff Schmising C, Pfau B, Schneider M, Günther CM, Giovannella M, Perron J, Vodungbo B, Müller L, Capotondi F, Pedersoli E, Mahne N, Lüning J, Eisebitt S. Imaging ultrafast demagnetization dynamics after a spatially localized optical excitation. Physical Review Letters. 2014;**112**:217203. doi:10.1103/PhysRevLett.112.217203

[27] Büttner F, Moutafis C, Bisig A, Wohlhüter P, Günther CM, Mohanty J, Geilhufe J, Schneider M, von Korff Schmising C, Schaffert S, Pfau B, Hantschmann M, Riemeier M, Emmel M, Finizio S, Jakob G, Weigand M, Rhensius J, Franken JH, Lavrijsen R, Swagten HJM, Stoll H, Eisebitt S, Kläui M. Magnetic states in low-pinning high-anisotropy material nanostructures suitable for dynamic imaging. Physical Review B. 2013;**87**:134422. doi:10.1103/PhysRevB.87.134422

[28] Büttner F Topological mass of magnetic Skyrmions probed by ultrafast dynamic imaging [thesis]. Mainz: University of Mainz; 2013.

[29] Dai D, Chen HW, Bowers JE, Kang Y, Morse M, Paniccia MJ. Equivalent circuit model of a Ge/Si avalanche photodiode. In: Group IV Photonics, 2009. GFP'09. 6th IEEE International Conference on, 9–11 September 2009.